analysed by SDS–PAGE and western blotting. Rabbit anti-ISWI antibody was biotinylated using the Clontech Biotin-X-NHS ester labelling kit. Detection was by streptavidin–peroxidase polymer (Sigma) with an ECL detection kit (Amersham).

Nucleosome spacing. *Drosophila* embryo assembly extract was dialysed against EX120, 0.2 mM PMSF, 0.5 mM sodium metabisulphite to remove ATP. 60 µl of extract, 66 µl EX50, 14 µl 30 mM $MgCl_2$, 10 mM DTT, 600 mM NaCl and 1 µg plasmid DNA were mixed and incubated for 3 h at 26 °C. Chromatin was Sarkosyl-stripped and purified by gel filtration[7,11]. 20 µl of this chromatin (~70 ng DNA) plus 30 µl EX120 were incubated for 90 min with either 1 µl CHRAC or buffer in presence or absence of 2 mM ATP. The nucleosome repeat was revealed with an oligonucleotide hybridizing to a GAGA element of the *hsp26* promoter as described[7,29]. 0.1 and 0.2 µl CHRAC and 1 µl NURF P11 (gift from T. Tsukiyama and C. Wu) were assayed in the experiment shown in Fig. 6b. The CHRAC preparation contained 5× more ISWI protein than the NURF preparation.

1. Kingston, R., Bunker, C. & Imbalzano, A. N. Repression and activation by multiprotein complexes that alter chromatin structure. *Genes Dev.* **10,** 905–920 (1996).
2. Felsenfeld, G. Chromatin unfolds. *Cell* **86,** 13–19 (1996).
3. Peterson, C. L. & Tamkun, J. W. The SWI–SNF complex: a chromatin remodelling machine? *Trends Biochem. Sci.* **20,** 143–146 (1995).
4. Tsukiyama, T. & Wu, C. Purification and properties of an ATP-dependent nucleosome remodelling factor. *Cell* **83,** 1011–1020 (1995).
5. Cairns, B. R. *et al.* RSC, an essential, abundant chromatin-remodelling complex. *Cell* **87,** 1249–1260 (1996).
6. Tsukiyama, T., Daniel, C., Tamkun, J. & Wu, C. ISWI, a member of the SWI2/SNF2 ATPase family, encodes the 140 kD subunit of the nucleosome remodelling factor. *Cell* **83,** 1021–1026 (1995).
7. Tsukiyama, T., Becker, P. B. & Wu, C. ATP-dependent nucleosome disruption at a heat-shock promoter mediated by binding of GAGA transcription factor. *Nature* **367,** 525–532 (1994).
8. Elfring, L. K., Deuring, R., McCallum, C. M., Peterson, C. L. & Tamkun, J. W. Identification and characterization of *Drosophila* relatives of the yeast transcriptional activator SNF2/SWI2. *Mol. Cell. Biol.* **14,** 2225–2234 (1994).
9. Becker, P. B. & Wu, C. Cell-free system for assembly of transcriptionally repressed chromatin from *Drosophila* embryos. *Mol. Cell. Biol.* **12,** 2241–2249 (1992).
10. Becker, P. B., Tsukiyama, T. & Wu, C. Chromatin assembly extracts from *Drosophila* embryos. *Meth. Cell Biol.* **44,** 207–223 (1994).
11. Varga-Weisz, P. D., Blank, T. A. & Becker, P. B. Energy-dependent chromatin accessibility and nucleosome mobility in a cell-free system. *EMBO J.* **14,** 2209–2216 (1995).
12. Wilm, M. *et al.* Femtomole sequencing of proteins from polyacrylamide gels by nano-electrospray mass spectrometry. *Nature* **379,** 466–469 (1996).
13. Mann, M. & Wilm, M. Error-tolerant identification of peptides in sequence databases by peptide sequence tags. *Analyt. Chem.* **66,** 4390–4399 (1994).
14. Berger, J. M., Gamblin, S. J., Harrison, S. C. & Wang, J. C. Structure and mechanism of DNA topoisomerase II. *Nature* **379,** 225–232 (1996).
15. Wang, W. D. *et al.* Diversity and specialization of mammalian SWI/SNF complexes. *Genes Dev.* **10,** 2117–2130 (1996).
16. Wang, J. C. DNA topoisomerases. *Annu. Rev. Biochem.* **65,** 635–692 (1996).
17. Almouzni, G. & Méchali, M. Assembly of spaced chromatin. Involvement of ATP and DNA topoisomerase activity. *EMBO J.* **7,** 4355–4365 (1988).
18. Walter, P. P., Owen-Hughes, T. A., Coté, J. & Workman, J. L. Stimulation of transcription factor binding and histone displacement by nucleosome assembly protein 1 and nucleoplasmin requires disruption of the histone octamer. *Mol. Cell. Biol.* **15,** 6178–6187 (1995).
19. Chen, G. L. *et al.* Nonintercalative antitumor drugs interfere with the breakage-reunion reaction of mammalian DNA topoisomerase II. *J. Biol. Chem.* **259,** 13560–13566 (1984).
20. Buchenau, P., Saumweber, H. & Arndt, J. D. Consequences of topoisomerase II inhibition in early embryogenesis of *Drosophila* revealed by *in vivo* confocal laser scanning microscopy. *J. Cell Sci.* **104,** 1175–1185 (1993).
21. Poljak, L. & Käs, E. Resolving the role of topoisomerase II in chromatin structure and function. *Trends Cell Biol.* **5,** 348–354 (1995).
22. Wartburton, P. E. & Earnshaw, W. C. Untangling the role of DNA topoisomerase II in mitotic chromosome structure and function. *BioAssays* **19,** 97–99 (1997).
23. Earnshaw, W. C., Halligan, B., Cooke, C. A., Heck, M. M. & Liu, L. F. Topoisomerase II is a structural component of mitotic chromosome scaffolds. *J. Cell Biol.* **100,** 1706–1715 (1985).
24. Gasser, S. M., Laroche, T., Falquet, J., Boy de la Tour, E. & Laemmli, U. K. Metaphase chromosome structure. Involvement of topoisomerase II. *J. Mol. Biol.* **188,** 613–629 (1986).
25. Swedlow, J. R., Sedat, J. W. & Agard, D. A. Multiple chromosomal populations of topoisomerase II detected *in vivo* by time-lapse, three-dimensional wide-field microscopy. *Cell* **73,** 97–108 (1993).
26. Sandaltzopoulos, R., Mitchelmore, C., Bonte, E., Wall, G. & Becker, P. B. Dual regulation of the *Drosophila hsp26* promoter *in vitro*. *Nucleic Acids Res.* **23,** 2479–2487 (1995).
27. Shevchenko, A., Wilm, M., Vorm, O. & Mann, M. Mass spectrometric sequencing of proteins from silver-stained polyacrylamide gels. *Analyt. Chem.* **68,** 850–858 (1996).
28. Wilm, M. & Mann, M. Analytical properties of the nanoelectrospray ion source. *Analyt. Chem.* **68,** 1–8 (1996).
29. Wall, G., Varga-Weisz, P. D., Sandaltzopoulos, R. & Becker, P. B. Chromatin remodelling by GAGA factor and heat shock factor at the hypersensitive *Drosophila hsp26* promoter *in vitro*. *EMBO J.* **14,** 1727–1736 (1995).

Correspondence and requests for materials should be addressed to P.B.B. (e-mail: becker@embl-heidelberg.de).

Modelling teleconnections between the North Atlantic and North Pacific during the Younger Dryas

Uwe Mikolajewicz, Thomas J. Crowley, Andreas Schiller & Reinhard Voss

In Figs 1 and 3b, the numbering was very faint; also, shading was lost from Fig. 4. The corrected figures 1, 3b and 4 are shown here. □
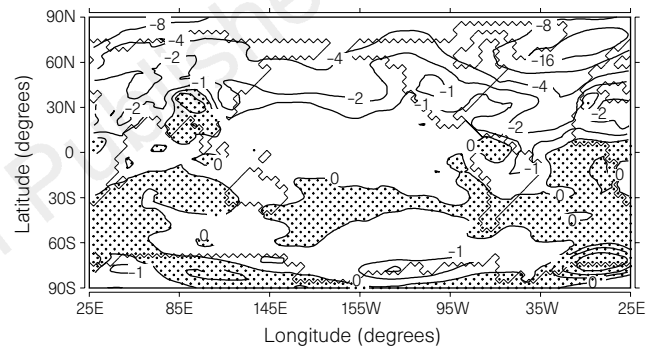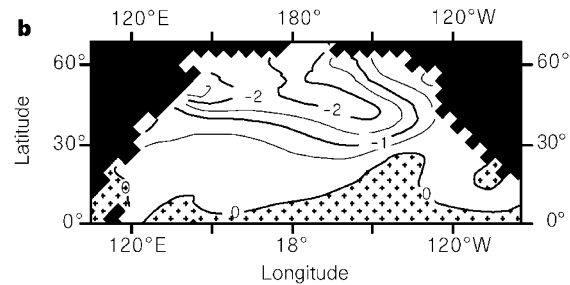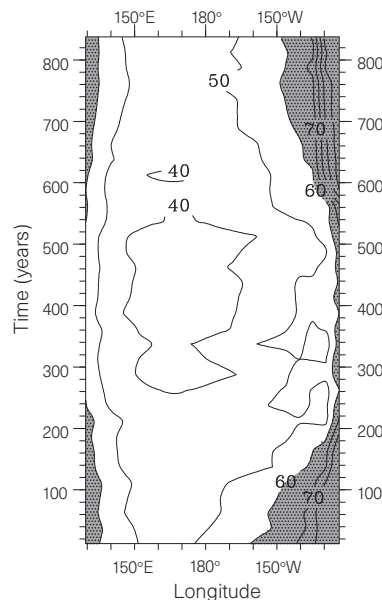

Figure 1

Figure 3

Figure 4

residue-based control can be exerted over α-peptide conformation by varying substitution at C_α, if backbone hydrogen-bonding sites are to remain intact[23–25]. One type of hydrogen-bonded helical secondary structure (α-helix) is predominant among peptides composed of the proteogenic α-amino acids, and the only other observed hydrogen-bonded helix (3_{10}) is relatively uncommon[26]. The switch in helical hydrogen-bond directionality between the β-peptide 12- and 14-helices (Fig. 1a) is unprecedented among α-peptides. The predictable residue-based conformational control offered by β-peptides suggests that this class of unnatural foldamers will be well suited to molecular design efforts, such as the generation of novel tertiary structures and combinatorial searches for selective biopolymer ligands. □

1. Ball, P. *Designing the Molecular World* (Princeton Univ. Press, Princeton, 1994).
2. Lehn, J.-M. *Supramolecular Chemistry: Concepts and Perspectives* (VCH, Weinheim, 1995).
3. Dado, G. P. & Gellman, S. H. Intramolecular hydrogen bonding in derivatives of β-alanine and γ-amino butyric acid: model studies for the folding of unnatural polypeptide backbones. *J. Am. Chem. Soc.* **116**, 1054–1062 (1994).
4. Hagihara, M., Anthony, N. J., Stout, T. J., Clardy, J. & Schreiber, S. L. Vinylogous polypeptides: an alternative peptide backbone. *J. Am. Chem. Soc.* **114**, 6568–6570 (1992).
5. Eschenmoser, A. Chemistry of potentially prebiological natural products. *Origins Life* **24**, 389–423 (1994).
6. Hamuro, Y., Geib, S. J. & Hamilton, A. H. Oligoanthranilamides. Non-peptide subunits that show formation of specific secondary structure. *J. Am. Chem. Soc.* **118**, 7529–7541 (1996).
7. Gennari, C., Salom, B., Potenza, D. & Williams, A. Synthesis of sulfonamido-pseudopeptides: new chiral unnatural oligomers. *Angew. Chem. Int. Edn Engl.* **33**, 2067–2069 (1994).
8. Lokey, R. S. & Iverson, B. L. Synthetic molecules that fold into a pleated secondary structure in solution. *Nature* **375**, 303–305 (1995).
9. Smith, A. B. *et al.* De novo design, synthesis and X-ray crystal structures of pyrrolinone-based β-strand mimetics. *J. Am. Chem. Soc.* **116**, 9947–9962 (1994).
10. Nowick, J. S., Mahrus, S., Smith, E. M. & Ziller, J. W. Triurea derivatives of diethylenetriamine as potential templates for the formation of artificial β-sheets. *J. Am. Chem. Soc.* **118**, 1066–1072 (1996).
11. Seebach, D. *et al.* β-Peptides: synthesis by Arndt–Eistert homologation with concomitant peptide coupling. Structure determination by NMR and CD spectroscopy and by X-ray crystallography. Helical secondary structure of a β-hexapeptide in solution and its stability towards pepsin. *Helv. Chim. Acta* **79**, 913–941 (1996).
12. Seebach, D. *et al.* Probing the helical secondary structure of short-chain β-peptides. *Helv. Chim. Acta* **79**, 2043–2066 (1996).
13. Appella, D. H., Christianson, L. A., Karle, I. L., Powell, D. R. & Gellman, S. H. β-Peptide foldamers: robust helix formation in a new family of β-amino acid oligomers. *J. Am. Chem. Soc.* **118**, 13071–13072 (1996).
14. Yuki, H., Okamoto, Y., Taketani, Y., Tsubota, T. & Marubayashi, Y. Poly(β-amino acid)s. IV. Synthesis and conformational properties of poly(α-isobutyl-L-aspartate). *J. Polym. Sci. Polym. Chem. Edn* **16**, 2237–2251 (1978).
15. Fernández-Santin, J. M., Aymamí, J., Rodríguez-Galán, A., Muñoz-Guerra, S. & Subirana, J. A. A pseudo α-helix from poly(α-isobutyl-L-aspartate), a nylon-3 derivative. *Nature* **311**, 53–54 (1984).
16. Fernández-Santin, J. M. *et al.* Helical conformations in a polyamide of the nylon-3 family. *Macromolecules* **20**, 62–68 (1987).
17. Bella, J., Alemán, C., Fernández-Santin, J. M., Alegre, C. & Subirana, J. A. Conformation of the helical polyamide poly(α-isobutyl-L-aspartate). *Macromolecules* **25**, 5225–5230 (1992).
18. López-Carrasquero, F., Alemá, C. & Muñoz-Guerra, S. Conformational analysis of helical poly(β-L-aspartate)s by IR dichroism. *Biopolymers* **36**, 263–271 (1995).
19. Herradon, B. & Seebach, D. Monoalkylation and dialkylation of derivatives of (1R, 2S)-2-hydroxycyclopentanecarboxylic acid and (1R, 2S)-2-hydroxycyclohexanecarboxylic acid via bicyclic dioxanones: selective generation of three contiguous stereocenters on a cyclohexane ring. *Helv. Chim. Acta* **72**, 690–714 (1989).
20. Tilley, J. W. *et al.* Analogs of Ac-CCK-7 incorporating dipeptide mimics in place of $Met^{29}–Gly^{29}$. *J. Med. Chem.* **35**, 3774–3783 (1992).
21. Braunschweiler, L. & Ernst, R. R. Coherence transfer by isotropic mixing: application to proton correlation spectroscopy. *J. Magn. Reson.* **53**, 521–528 (1983).
22. Bothner-By, A. A., Stephens, R. L., Lee, J., Warren, C. D. & Jeanloz, R. W. Structure determination of a tetrasaccharide: transient nuclear Overhauser effects in the rotating frame. *J. Am. Chem. Soc.* **106**, 811–813 (1984).
23. Creighton, T. E. *Proteins: Structures and Molecular Properties*, 2nd Edn (Freeman, New York, 1993).
24. Xiong, H., Buckwalter, B. L., Shieh, H.-M. & Hecht, M. H. Periodicity of polar and nonpolar amino acids is the major determinant of secondary structure in self-assembling oligomeric peptides. *Proc. Natl Acad. Sci. USA* **92**, 6349–6353 (1995).
25. Schenck, H. L., Dado, G. P. & Gellman, S. H. Redox-triggered secondary structure changes in the aggregated states of a designed methionine-rich peptide. *J. Am. Chem. Soc.* **118**, 12487–12494 (1996).
26. Barlow, D. J. & Thornton, J. M. Helix geometry in proteins. *J. Mol. Biol.* **201**, 601–619 (1988).
27. Bacon, D. J. & Anderson, W. F. A fast algorithm for rendering space-filling molecule pictures. *J. Mol. Graphics* **6**, 219–220 (1988).
28. Merrit, E. A. & Murphy, M. E. P. Raster3D version 2.0: a program for photorealistic molecular graphics. *Acta Cryst.* D**50**, 869–873 (1994).
29. Kraulis, P. J. Molscript: a program to produce both detailed and schematic plots of protein structures. *J. Appl. Cryst.* **24**, 946–950 (1991).
30. Brooks, B. R. *et al.* CHARMM: a program for macromolecular energy, minimization, and dynamics calculations. *J. Comput. Chem.* **4**, 187–217 (1983).

Modelling teleconnections between the North Atlantic and North Pacific during the Younger Dryas

Uwe Mikolajewicz*, **Thomas J. Crowley**†, **Andreas Schiller**‡ & **Reinhard Voss**§

* *Max-Planck-Institut für Meteorologie, D-20146 Hamburg, Germany*
† *Department of Oceanography, Texas A&M University, College Station, Texas 77843, USA*
‡ *CSIRO Division of Marine Research, Hobart TAS 7001, Australia*
§ *Deutsches Klimarechenzentrum, D-20146 Hamburg, Germany*

Evidence for a cooling event synchronous with the Younger Dryas (12,000 calendar years before present) has been found in the North Pacific Ocean north of 30° N in records of surface[1–5] and subsurface water properties[6,7]. These changes may be related to a temporary shut-down of North Atlantic Deep Water formation and associated surface cooling over the North Atlantic. It has remained unclear, however, whether this North Atlantic cooling was communicated to the North Pacific Ocean through the atmosphere or the ocean. Here we report results of a sensitivity experiment with a coupled ocean–atmosphere general circulation model that support a primarily atmospheric forcing of North Pacific climate variations. Changes in wind strongly affect coastal upwelling at the North American west coast, and surface cooling by the atmosphere causes better ventilation of the thermocline waters of the northeast Pacific. This effect is amplified by oceanic progagation to the Pacific of the signal arising from collapse of North Atlantic Deep Water formation. These teleconnections may also explain earlier North Pacific and western North American millenial-scale cooling events of a similar nature[8–12].

Previous modelling results indicate that meltwater-induced changes in subpolar North Atlantic salinity affects North Atlantic Deep Water (NADW) production (see, for example, refs 13–18). Although most of the analyses of these runs have focused on the North Atlantic and surroundings, less attention has been paid to the far-field effect of meltwater-induced NADW decreases. Generally this effect is significantly smaller than in the North Atlantic. The model[18] used here shows a maximum cooling over the North Atlantic and Europe, but almost the entire Northern Hemisphere experiences a marked cooling (Fig. 1). This response is more extensive than that obtained with a different coupled model[17], but the brevity of the meltwater forcing in that run (10 years) does not make the two studies strictly comparable. However, an equilibrium run[19] with a rather similar model results in a response quite similar to ours. From simulations with less complete models[15,20,21], enhanced formation of intermediate water in the North Pacific has been reported as a consequence of the shutdown of NADW formation.
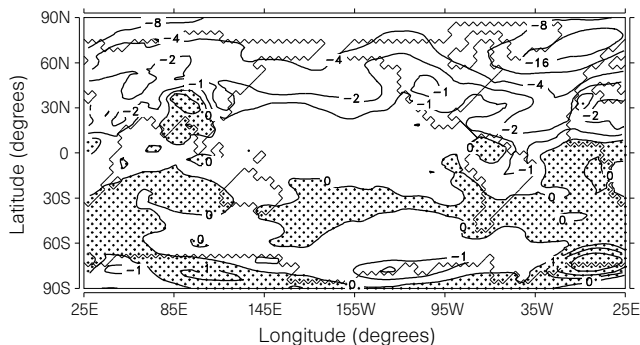
The model used here is the ECHAM3/LSG coupled ocean–atmosphere general circulation model (OAGCM) consisting of the spectral atmosphere model ECHAM3[22] with a T21 resolution and 19 levels, and the LSG ocean model[23] with a horizontal resolution of 5.6° and 11 levels. The two model components are coupled by the fluxes of heat, mass and momentum, making use of the flux correction technique. Both components of the OAGCM are periodically synchronously coupled. Periods with synchronous coupling (both models are integrated quasi-simultaneously) of 15 months alternate with ocean-only periods of 48 months[24]. This technique saves considerable amounts of computer time, while retaining the response on timescales longer than a few decades. A

more detailed description of the coupled model and its climate can be found elsewhere[18,25].

In a sensitivity experiment we investigated the stability of the thermohaline circulation against meltwater input into the Labrador Sea, keeping all other boundary conditions (such as topography, vegetation and ice sheets) at modern values. The prescribed triangular-shaped meltwater spike lasted for 500 years and reached a maximum of 0.625 Sv (1 Sv = 10^6 m^3 s^{-1}) in year 250. The total length of this experiment and of an unperturbed control run is 850 model years. This experimental set-up mimics a meltwater event originating from the Laurentide ice sheet over North America. The prescribed discharge rates are roughly consistent with the estimates of the maximum rate of change of global mean sea level during the last deglaciation[26]. But this model, like other models (for example, refs 14, 17, 20) fails to reproduce the delay of about 1,000 years between the peak of the meltwater input and the onset of the Younger Dryas.

As discussed more fully in ref. 18, the meltwater input into the Labrador Sea reduced the model's surface salinity in the northern North Atlantic, and thus formation of NADW ceased (Fig. 2a). As a result, the thermohaline circulation of the Atlantic was reversed, accompanied by a strong reduction of the North Atlantic poleward heat transport (at 30° N) from 0.7 PW to 0.1 PW (1PW = 10^{15} W). This leads to a strong surface cooling over the North Atlantic and Europe (Fig. 1) and to increased sea-ice cover. The sea surface temperature (SST) cools by almost 4 K averaged over the entire North Atlantic (Fig. 2b). After the meltwater input was stopped, the convection slowly recovered, and the Atlantic circulation returned to the conveyor-belt type overturning pattern. The North Atlantic SST warms up within a few decades by 2.5 K (Fig. 2b).

Although the meltwater responses have maximal amplitude in the Atlantic and Europe, the signal is distinct in the Pacific as well (Fig. 1). Sea surface temperature, averaged over the entire North Pacific, shows a marked cooling, with maximal amplitude of ~2 K in the third century of the simulation (Fig. 2b). The temperature changes are not as abrupt as in the Atlantic, but the reinitiation of NADW formation shows up as a warming of 1 K within one century. The strong changes in SST and sea-ice distribution lead also to significant changes in the atmospheric circulation. The first empirical orthogonal function (EOF) of the wind stress fields of the Northern Hemisphere Pacific shows a strong cyclonic signal centred around 60° N and 155° W, with westerlies extending across

the Pacific around 45° N. There is a strong northward component along the Canadian and US west coast and a weaker westward component at the Mexican coast (Fig. 3a). The pattern is consistent with an eastward shift in the position of the Aleutian low-pressure area and the intensification of cyclone activity, especially in the eastern part of the North Pacific. The associated principle component (PC) time series (Fig. 2c) shows marked differences to the control run between years 150 and 530 that are clearly related to changes in the Atlantic overturning circulation.

The divergence of the resulting Ekman transports causes anomalous upwelling in the Pacific north of 50° N during periods of suppressed NADW formation. At the west coast of North America, however, the northward wind-stress anomaly causes a convergence of Ekman transports and thus anomalous downwelling along the coast. The corresponding negative anomaly of the vertical velocities extends down to depths of 850 m. At 1,500 m, however, the anomaly changes sign and shows an upward component in the northeast Pacific. The pattern of the associated response in SST (Fig. 3b) reveals a general cooling of the North Pacific north of 30° N. Maximal cooling (~2 K) can be seen in a tongue around 50° N extending from 140° E to 150° W. This pattern corresponds with an enhanced cold-air advection from Siberia, especially in the winter season. The relatively small cooling at the American coast coincides with the intensification of the northward-blowing winds along the coast and the reduction of the upwelling of colder subsurface waters south of 40° N.

In an uncoupled sensitivity experiment with the ECHAM3 atmosphere model, the SST and sea ice were prescribed according to the meltwater experiment in the Atlantic and to the control run elsewhere. The atmospheric response over the Atlantic and Eurasia (not
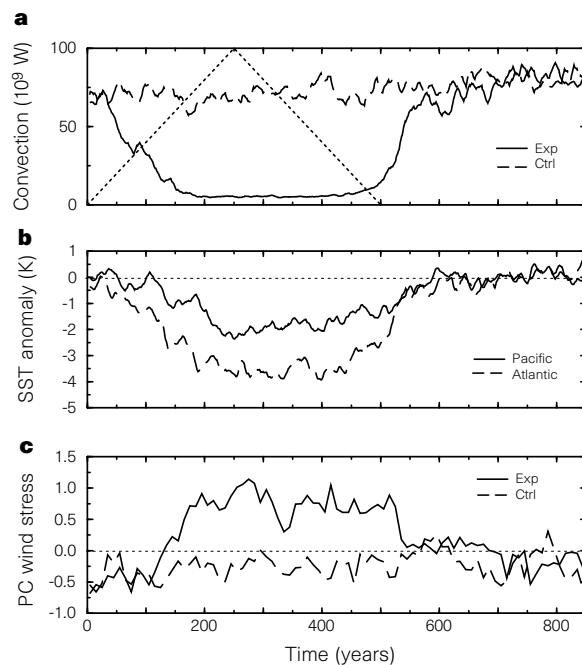

Figure 1 Change in decadal mean near-surface air temperature in the case of a shutdown of North Atlantic Deep Water formation in the ECHAM3/LSG coupled OAGCM. Displayed are the mean differences between two 10-year synchronous integrations corresponding to years 241 to 250 from both meltwater experiment and control run (see text). Details of the experiments are described in ref. 18 and time series of integral quantities are shown in Fig. 2. Isolines are plotted for ±0, 1, 2, 4, 8 and 16 K. Stippling indicates higher temperatures in the meltwater experiment. Note significant cooling in the North Pacific north of 30–40° N.


Figure 2 Time series (850 years) from meltwater experiment (Exp) and control run (Ctrl). All data are decadal mean data without further filtering. **a**, Convection in North Atlantic and Arctic (an indicator of the actual NADW formation rate) and a schematic illustration of the prescribed meltwater input (dotted line) with a maximum of 0.625 Sv in year 250. **b**, SST anomalies between meltwater experiment and control. The solid line shows the SST averaged over the Pacific north of 30° N. The dashed line shows the time series averaged in the Atlantic between 30° and 70° N. Locally the annual mean cooling reaches maxima of more than 8 K. **c**, Principal component (PC) time series of the wind stress EOF shown in Fig. 3a.

shown) was very similar to the response in the meltwater experiment (Fig. 1). The atmosphere extracted large amounts of heat near the northwest Pacific coast due to the outflow of colder air from Siberia in winter. During the period of cooling around year 200 in the coupled simulation, the annual mean heat loss from the North Pacific Ocean to the atmosphere increased by 0.2 PW compared to the control experiment. During the rest of the cold period this additional heat loss is reduced to 0.1 PW. Thus the North Pacific cooling is a direct consequence of the climate changes in the North Atlantic. The changes in atmospheric circulation over the North Pacific found in the meltwater experiment is a combination of the far-field response from the Atlantic and the local interaction with the increased meridional SST gradient over the North Pacific.

In the coupled model, the cooling in the surface layer also leads to an intensified ventilation of the thermocline in the North Pacific, as was already found previously in a zonally averaged model[20]. Especially in the northeast Pacific, the wintertime mixed layer depth is increased. The ventilation of the thermocline produces a tongue of colder and fresher water which penetrates deeper and further to the south than in the control simulation before it leaves the coast flowing westward. In the zonally averaged mass-transport stream function this shows up as an increase of 3 Sv of the North Pacific Intermediate Water formation (not shown). We illustrate the effect of the circulation changes on the ventilation using an offline

advective tracer model for radiocarbon[14]. The temporal evolution of the resulting difference in $\Delta^{14}C$ between the surface and 450 m depth (approximately sill depth in the Santa Barbara basin[6]) along 35° N in the Pacific is shown in Fig. 4. Along the American coast, the reduction of the $\Delta^{14}C$ differences is almost 30‰. This can be explained by the combined effect of wind-induced reduction of the upwelling of old deep water and the deeper penetration of young water. This signal is consistent with the changes found by Kennett and Ingram[6], except that our model overestimates the ventilation age. In the model, the radiocarbon signal at the coast at 450 m depth is associated with a cooling and freshening (~0.8 K and 0.4 practical salinity units). There is, however, a strong depth dependence of the radiocarbon signal near the coast. At the next model level (250 m depth) the $\Delta^{14}C$ difference with the surface is reduced by 25‰ during the cold period. At 2,000 m depth, the radiocarbon concentrations indicate an increase in ^{14}C depletion along the American coast, but with a clear delay compared to the surface response. This depth-dependent pattern of ventilation changes appears to be consistent with new data from deeper sites in the northeast Pacific.[7] However, for comparison with observed data, one also must take into account that the atmospheric radiocarbon concentration increased ~35‰ during the Younger Dryas[27]. This response has been successfully simulated with simplified coupled models[21,28]

In a sensitivity experiment with the uncoupled ocean model with
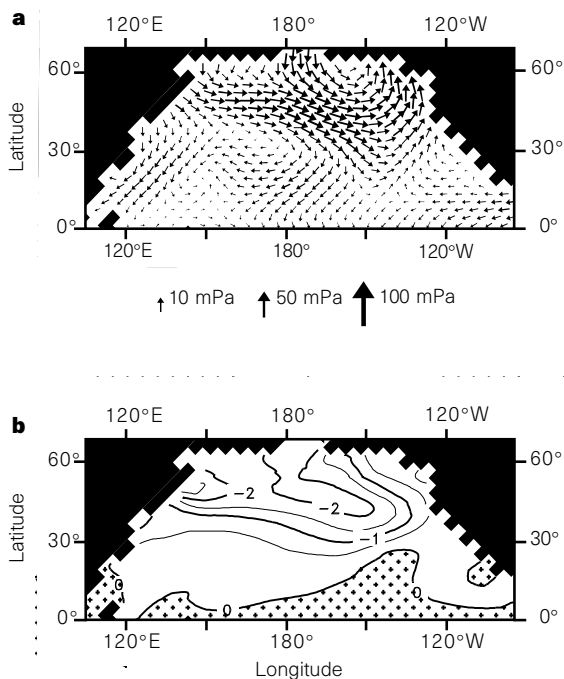
Figure 3 a, First common EOF (explains 38.5% of total variance) of Northern Hemisphere Pacific wind stress from both control and meltwater experiment and **b**, associated correlation pattern of SST (in K). Decadal means of the data from both the meltwater experiment and the control run were used for this analysis. The common time-mean value from both experiments was subtracted before the analysis. To obtain the strength of the anomaly for any particular time interval of the simulation, both patterns must be multiplied by the difference of the loading of the principal component (PC) shown in Fig. 2c. The pattern is strongest in the winter season. The change in SST associated with this response was computed by linear regression analysis with the PC of the wind stress EOF. As the wind stress pattern is directly related to the SST in the North Atlantic, this pattern shows the combined effect of the advection of colder air from Siberia (compare with Fig. 1) onto the North Pacific and the temperature effects associated with changes in the atmospheric circulation.
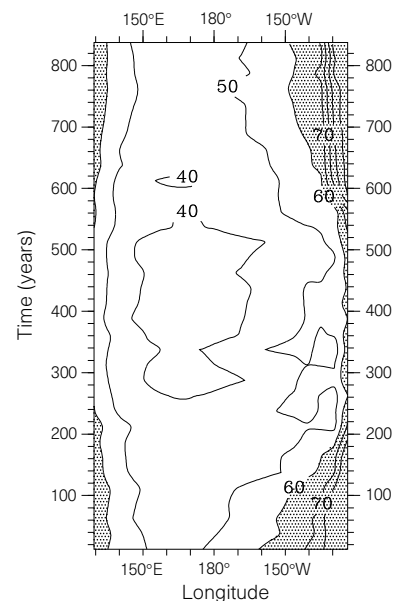
Figure 4 Hovmøller diagram of radiocarbon ($\Delta^{14}C$) differences between surface and 450 m depth at 35° N in the Pacific from an advective tracer model. ($\Delta^{14}C$ is defined as the deviation of the $^{14}C/^{12}C$ ratio from a given standard and corrected for fractionation effects, given in ‰). Shown are averages over 25 years of the meltwater experiment; contour interval is 10‰. Shading indicates values >60‰. The results are obtained using an offline advective tracer model, which was spun-up by making a sequence of twenty 850-year integrations using the flow fields from the individual years of the control run. Each run was started with the $\Delta^{14}C$ field achieved at the end of the previous simulation. The model was then forced with flow fields from the 850 years of the meltwater experiment. As the change in surface concentrations at this latitude was generally <10‰ and showed younger radiocarbon values during the cold period, the reduction in $\Delta^{14}C$ difference by ~10‰ over the whole Pacific reflects mainly changes at 450 m depth. Further south (for example, at 28° N) the model shows a similar increase in the ventilation of the central Pacific, but changes in coastal areas are not as large.

a restoring time constant of 5 months for the surface temperature[16], a collapse of NADW formation induced by the introduction of a large negative salinity anomaly in the North Atlantic leads also to enhanced ventilation of the thermocline with fresher water (with signal propagation by coastal and equatorial Kelvin and Rossby waves within less than three decades from the Atlantic through the Indian Ocean to the northeast Pacific). However, this mechanism (compare ref. 6) accounts for only about one-third of the radiocarbon signal in the OAGCM. The remaining part thus can be explained by effects caused by changes in the atmosphere.

Although there is some agreement between model and geological data for circulation changes along the American west coast, there are also some disagreements. The cooling near the coast in our model is rather small (~1 K), whereas sediment records suggest[6,29] a surface cooling of 2–3 K. Because there is some discrepancy between alkenone-based and foraminifera-based (*Globigerina pachyderma*) SST estimates for the Last Glacial Maximum from the Santa Barbara basin[6,29], and *G. pachyderma* may have a subsurface habitat[30], the upwelling 'discrepancies' may not necessarily reflect model inadequacies. The large changes in land ice cover, which are not included in our simulations, would also influence the circulation response. Another important shortcoming of the simulations is the coarse resolution (both horizontally and vertically) which makes the comparison with local phenomena in regions with large topography gradients questionable and does not allow the simulation of several important small-scale features. To address the above discrepancies a more complete set of experiments would be required with fully realistic boundary conditions for the deglacial.

Despite the differences mentioned above, our results clearly demonstrate the influence of variations in NADW formation on the North Pacific. In the case of a collapse of NADW formation, both the atmospheric and oceanic transmission of the signal lead to enhanced ventilation of the northeast Pacific thermocline, with the atmospheric effect about twice as strong as the oceanic. These results explain concurrent changes in the North Atlantic and North Pacific for both the Younger Dryas and (possibly) earlier millenial-scale cooling events of a similar nature[9–12]. Owing to the atmospheric teleconnection, a cooling in the North Atlantic and increased sea-ice cover alone seem to be sufficient to enhance thermocline variation in the northeast Pacific. □

1. Heusser, C. J. *Late Pleistocene Environments of North Pacific and North America* (Spec. Publ. 35, Geogr. Soc., New York, 1960).
2. Peteet, D. M. & Mann, D. H. Late-glacial vegetation, tephra, and climatic history of southwestern Kodiak Island, Alaska. *Ecoscience* **1**, 255–267 (1994).
3. Peteet, D. M. Global Younger Dryas? *Quat. Int.* **38**, 93–104 (1995).
4. Kallel, N. *et al.* Evidence of cooling during the Younger Dryas in the western North Pacific. *Oceanol. Acta* **11**, 369–375 (1988).
5. Keigwin, L. D. & Jones, G. A. Deglacial climatic oscillations in the Gulf of California. *Paleoceanography* **5**, 1009–1023 (1990).
6. Kennett, J. P. & Ingram, B. L. A 20,000-year record of ocean circulation and climate change from the Santa Barbara Basin. *Nature* **377**, 510–514 (1995).
7. van Geen, A. *et al.* Ventilation changes in the northeast Pacific during the last deglaciation. *Paleoceanography* **11**, 519–528 (1996).
8. Thunell, R. C. & Mortyn, P. G. Glacial climate instability in the Northeast Pacific Ocean. *Nature* **376**, 504–506 (1995).
9. Behl, R. J. & Kennett, J. P. Brief interstadial events in the Santa Barbara Basin, NE Pacific, during the past 60 kyr. *Nature* **379**, 243–246 (1996).
10. Kotilainen, A. T. & Shackleton, N. J. Rapid climate variability in the North Pacific during the past 95,000 years. *Nature* **377**, 323–326 (1995).
11. Benson, L. V. *et al.* Climatic and hydrologic oscillations in the Owens Lake Basin and adjacent Sierra Nevada, California. *Science* **274**, 746–749 (1996).
12. Philips, F. M. *et al.* Chronology for fluctuations in Late Pleistocene Sierra Nevada glaciers and lakes. *Science* **274**, 749–751 (1996).
13. Rooth, C. Hydrology and ocean circulation. *Prog. Oceanogr.* **11**, 131–149 (1982).
14. Maier-Reimer, E. & Mikolajewicz, U. in *Oceanography 1988* (eds Ayala-Castañares, A., Wooster, W. & Yáñez-Arancibia, A.) 87–100 (UNAM, Mexico, 1989).
15. Rahmstorf, S. Bifurcations of the Atlantic thermohaline circulation in response to changes in the hydrological cycle. *Nature* **378**, 145–149 (1995).
16. Mikolajewicz, U. & Maier-Reimer, E. Mixed boundary conditions in ocean general circulation models and their influence on the stability of the model's conveyor-belt. *J. Geophys. Res.* **99**, 22633–22644 (1994).
17. Manabe, S. & Stouffer, R. J. Simulation of abrupt climate change induced by freshwater input to the North Atlantic Ocean. *Nature* **378**, 165–167 (1995).
18. Schiller, A., Mikolajewicz, U. & Voss, R. The stability of the North Atlantic thermohaline circulation in a coupled ocean-atmosphere general circulation model. *Clim. Dyn.* (in the press).
19. Manabe, S. & Stouffer, R. J. Two stable equilibria of a coupled ocean-atmosphere model. *J. Clim.* **1**, 941–866 (1988).
20. Wright, D. G. & Stocker, T. F. *Ice in the Climate System* (ed. Peltier, W. R.) 395–416 (Springer, Berlin, 1993).
21. Stocker, T. F. & Wright, D. G. Rapid changes in ocean circulation and atmospheric radiocarbon. *Paleoceanography* **11**, 773–795 (1996).
22. Roeckner, E. *et al.* Simulation of the present-day climate with the ECHAM model: impact of model physics and resolution. (Tech. Rep. No 93, Max-Planck-Inst. für Meteorologie, Hamburg, 1992).
23. Maier-Reimer, E., Mikolajewicz, U. & Hasselmann, K. Mean circulation of the LSG OGCM and its sensitivity to the thermohaline surface forcing. *J. Phys. Oceanogr.* **23**, 731–757 (1993).
24. Voss, R. & Sausen, R. Techniques for asynchronous and periodically synchronous coupling of atmosphere and ocean models. Part II: impact of variability. *Clim. Dyn.* **12**, 605–614 (1996).
25. Voss, R., Sausen, R. & Cubasch, U. Periodically synchronously coupled integrations with the atmosphere-ocean general circulation model ECHAM3/LSG. *Clim. Dyn.* (submitted).
26. Fairbanks, R. G. A 17,000-year glacio-eustatic sea level record: influence of glacial melting rates on the Younger Dryas event and deep-ocean circulation. *Nature* **342**, 637–642 (1989).
27. Goslar, T. *et al.* High concentration of atmospheric ^{14}C during the Younger Dryas cold episode. *Nature* **377**, 414–417 (1995).
28. Mikolajewicz, U. A meltwater induced collapse of the 'conveyor belt' thermohaline circulation and its influence on the distribution of Δ^{14}C and δ^{18}O in the oceans. (Tech. Rep. 189, Max-Planck-Inst. für Meteorologie, 1996).
29. Herbert, T. D., Yasuda, M. & Burnett, C. Glacial-interglacial sea-surface temperature record inferred from alkenone unsaturation indices, site 893, Santa Barbara Basin. *Proc. ODP* **146** (pt 2), 257–264 (1995).
30. Sautter, L. R. & Thunell, R. C. Seasonal variability in the δ^{18}O and δ^{13}C of planktonic foraminifera from an upwelling environment: Sediment trap results from the San Pedro Basin, Southern California Bight. *Paleoceanography* **6**, 307–334 (1991).

Catastrophic collapse at stratovolcanoes induced by gradual volcano spreading

B. van Wyk de Vries & P. W. Francis

Department of Earth Sciences, The Open University, Walton Hall, Milton Keynes, UK

Unlike ordinary mountains, which are formed by slow uplift and erosion, volcanoes are constructed rapidly. As a consequence, many are liable to massive flank failures, leading to debris avalanches (for example, at Mount St Helens in 1980). Such failures occur worldwide about once every 25 years (ref. 1) and even small ones can present a major hazard—in particular if far-reaching tsunamis are generated, as at Mayu-yama in 1792 (ref. 2). Previous work has tended to emphasize differences in eruption style associated with flank failure[2], but here we focus on the fundamental structural causes of failure. Most volcanic failures are generated by magmatic intrusion and flank spreading[3]. We present evidence, however, that Mombacho volcano in Nicaragua experienced a previously unrecognized type of failure, triggered by sub-volcanic basement spreading. Notably, collapses related to basement spreading do not require that the volcano be magmatically active, and thus flank failure may pose a significant risk even at inactive volcanoes, which are rarely monitored.

Mombacho volcano rises 1,400 m above the west shores of Lake Nicaragua, on a basement of Quaternary ignimbrite of the Las Sierras Formation[4,5] (Fig. 1). Conspicuous debris avalanche deposits on two sides of the volcano provide unequivocal evidence for recent flank failure. One deposit, below a well defined collapse scar, forms the remarkable Las Isletas archipelago in Lake Nicaragua (Fig. 1). The other, on the south side below the deep 'El Crater' scar, covers ~60 km² with hummocky avalanche deposit (Fig. 2). Forest cover indicates that the avalanche deposits are at least 1,000 years old. The 20,000-yr-old Apoyo pumice underlies the deposits, giving a maximum age[6].

Volcano spreading provides a framework to interpret the structural and magmatic evolution of volcanoes[7–9]. We propose here a new failure mode caused by lateral displacement of sub-volcanic strata. A similar process has been proposed for the Hawaiian shield